



## Article

# Highly Ordered SnO<sub>2</sub> Nanopillar Array as Binder-Free Anodes for Long-Life and High-Rate Li-Ion Batteries

Liyufen Dai<sup>1,2</sup>, Xiangli Zhong<sup>2</sup>, Juan Zou<sup>1,2</sup>, Bi Fu<sup>1</sup>, Yong Su<sup>2</sup>, Chuanlai Ren<sup>1</sup>, Jinbin Wang<sup>2</sup>  
and Gaokuo Zhong<sup>1,\*</sup> 

<sup>1</sup> Shenzhen Key Laboratory of Nanobiomechanics, Shenzhen Institutes of Advanced Technology, Chinese Academy of Sciences, Shenzhen 518055, China; lyf.dai@siat.ac.cn (L.D.); zjuan@xtu.edu.cn (J.Z.); fub@sustech.edu.cn (B.F.); cl.ren@siat.ac.cn (C.R.)

<sup>2</sup> School of Materials Science and Engineering, Xiangtan University, Xiangtan 411105, China; xlzhong@xtu.edu.cn (X.Z.); susu0324@163.com (Y.S.); jbwang@xtu.edu.cn (J.W.)

\* Correspondence: gk.zhong@siat.ac.cn

**Abstract:** SnO<sub>2</sub>, a typical transition metal oxide, is a promising conversion-type electrode material with an ultrahigh theoretical specific capacity of 1494 mAh g<sup>-1</sup>. Nevertheless, the electrochemical performance of SnO<sub>2</sub> electrode is limited by large volumetric changes (~300%) during the charge/discharge process, leading to rapid capacity decay, poor cyclic performance, and inferior rate capability. In order to overcome these bottlenecks, we develop highly ordered SnO<sub>2</sub> nanopillar array as binder-free anodes for LIBs, which are realized by anodic aluminum oxide-assisted pulsed laser deposition. The as-synthesized SnO<sub>2</sub> nanopillar exhibit an ultrahigh initial specific capacity of 1082 mAh g<sup>-1</sup> and maintain a high specific capacity of 524/313 mAh g<sup>-1</sup> after 1100/6500 cycles, outperforming SnO<sub>2</sub> thin film-based anodes and other reported binder-free SnO<sub>2</sub> anodes. Moreover, SnO<sub>2</sub> nanopillar demonstrate excellent rate performance under high current density of 64 C (1 C = 782 mA g<sup>-1</sup>), delivering a specific capacity of 278 mAh g<sup>-1</sup>, which can be restored to 670 mAh g<sup>-1</sup> after high-rate cycling. The superior electrochemical performance of SnO<sub>2</sub> nanopillar array can be attributed to the unique architecture of SnO<sub>2</sub>, where highly ordered SnO<sub>2</sub> nanopillar array provided adequate room for volumetric expansion and ensured structural integrity during the lithiation/delithiation process. The current study presents an effective approach to mitigate the inferior cyclic performance of SnO<sub>2</sub>-based electrodes, offering a realistic prospect for its applications as next-generation energy storage devices.

**Keywords:** lithium-ion batteries; SnO<sub>2</sub>; nanoarray; anode; high-rate



**Citation:** Dai, L.; Zhong, X.; Zou, J.; Fu, B.; Su, Y.; Ren, C.; Wang, J.; Zhong, G. Highly Ordered SnO<sub>2</sub> Nanopillar Array as Binder-Free Anodes for Long-Life and High-Rate Li-Ion Batteries. *Nanomaterials* **2021**, *11*, 1307. <https://doi.org/10.3390/nano11051307>

Academic Editors: Luca Pasquini and Sergio Brutti

Received: 17 March 2021

Accepted: 7 May 2021

Published: 15 May 2021

**Publisher's Note:** MDPI stays neutral with regard to jurisdictional claims in published maps and institutional affiliations.



**Copyright:** © 2021 by the authors. Licensee MDPI, Basel, Switzerland. This article is an open access article distributed under the terms and conditions of the Creative Commons Attribution (CC BY) license (<https://creativecommons.org/licenses/by/4.0/>).

## 1. Introduction

Rechargeable lithium-ion batteries (LIBs) enjoy superior energy density and high portability, realizing their widespread utilization in our commonly used electronic devices, such as mobile phones, cameras, and laptops [1]. In the last decade, the utilization of rechargeable LIBs has rapidly expanded into the field of electric vehicles (EVs) [2]. The development of next-generation EVs requires LIBs with excellent energy density and rapid charge/discharge capability under high current densities. Currently, the commercialization of LIBs is mainly based on the carbon anodes with graphitic layered structure [3], however, the limited theoretical capacity (372 mAh g<sup>-1</sup>) of graphite cannot meet the requirements of next-generation LIBs, driving the exploration of alternative anode materials with high Li storage capacity. Among a wide array of anode materials, transition metal oxides (TMOs) are considered promising candidates against commercial graphite due to its rich in natural resources and outstanding Li storage capacity [4,5]. In general, the Li-storage mechanism in TMOs is either intercalation/deintercalation ( $M_xO_y + nLi^+ + ne^- \leftrightarrow Li_nM_xO_y$ ) or conversion reaction ( $M_xO_y + 2yLi^+ + 2ye^- \leftrightarrow yLi_2O + xM$ ) [6]. One should note that the conversion-type TMOs render high theoretical Li storage capacity, such as Fe<sub>3</sub>O<sub>4</sub>

(926 mAh g<sup>-1</sup>) [7], Co<sub>3</sub>O<sub>4</sub> (890 mAh g<sup>-1</sup>) [8], and SnO<sub>2</sub> (1494 mAh g<sup>-1</sup>) [9]. However, the conversion-type TMOs experience large volumetric change during the charge/discharge process, e.g., the volume change of SnO<sub>2</sub> by ~300% [10,11], resulting in rapid capacity decay, inferior cyclic performance, and poor rate capability.

After the first report on the utilization of SnO<sub>2</sub> as an anode in LIBs by Idota et al. in 1997 [12], extensive research has been carried out to solve the problem of volumetric expansion [13–15]. Benefiting from the development of nanotechnology and nanoscience [16–18], a wide variety of SnO<sub>2</sub> nanostructures, such as nanorods [19], nanowires [20,21], nanotubes [22], and nanofibers [23], have been employed to improve the electrochemical performance and cyclic stability of SnO<sub>2</sub>-based anodes. Nevertheless, these nanostructures of SnO<sub>2</sub> suffer from the problems of agglomeration, redundant interfaces, and limited electron transfer [24]. Hence, a highly ordered and stable SnO<sub>2</sub> nanostructure is desired to overcome these problems. Herein, we have fabricated highly arrayed SnO<sub>2</sub> nanopillar by anodic aluminum oxide (AAO)-assisted pulsed laser deposition (PLD) and employed as an anode electrode in LIBs. Benefiting from the unique nanoarray structure, the SnO<sub>2</sub> anode rendered a reversible specific capacity of about 830 mAh g<sup>-1</sup> after 300 charge/discharge cycles and maintained a specific capacity of 313 mAh g<sup>-1</sup> after 6500 charge/discharge cycles at the current density of 2 C, exhibiting superior Li storage capacity and excellent cyclic life. Note that 1 C indicates the current strength of the battery when it is fully discharged in one hour, and 1 C of SnO<sub>2</sub> is 782 mA g<sup>-1</sup>. Furthermore, it shows the discharge capacity of 433, 414, 354, and 278 mAh g<sup>-1</sup> at the current density of 8, 16, 32, and 64 C, respectively, indicates the ultrahigh rate capability of as-synthesized SnO<sub>2</sub> nanopillar. These results reveal the superior electrochemical performance of highly arrayed SnO<sub>2</sub> nanopillar, which can be employed as binder-free electrodes in next-generation energy storage devices.

## 2. Materials and Methods

### 2.1. SnO<sub>2</sub> Nanopillar Array Deposition

In order to improve the hydrophilicity of Cu foil surface and the adhesion between the AAO template and Cu foil, a plasma cleaning system was used to clean the surface of Cu foil before the transfer of AAO template. The employed AAO templates were purchased from Topmembranes Technology Co., LTD, and their thickness and aperture are around 650 nm and 310 nm, respectively. The fabrication of SnO<sub>2</sub> nanopillar array included three steps: (1) transfer of AAO template, (2) SnO<sub>2</sub> deposition, and (3) removal of AAO template. AAO-covered Cu foil and bare Cu foil were placed in a PLD system (Pascal Mobile Combi-Laser MBE) to deposit SnO<sub>2</sub>. The optimal deposition conditions were achieved by setting the laser energy at 350 mJ, laser pulse frequency at 10 Hz, substrate temperature at 500 °C and oxygen pressure at  $2.0 \times 10^{-6}$  Torr. The removal of the AAO template was accomplished by using polyimide high-temperature adhesive tape.

### 2.2. Electrochemical Characterization

The SnO<sub>2</sub> nanoarray and thin-film electrodes (0.5 cm × 0.5 cm) with a mass loading of 0.12 mg/cm<sup>2</sup> and 0.2 mg/cm<sup>2</sup>, respectively, were used for electrochemical characterization. The CR2025-type coin-cells were assembled in an Ar-filled gloves box with water and oxygen content of < 0.2 ppm. The 1 M electrolyte was prepared by adding an appropriate amount of LiPF<sub>6</sub> to the mixed solution of ethylene carbonate (EC) and dimethyl carbonate (DMC) (1:1 v/v). The involved separator material is PP (polypropylene) /PE (polyethylene) /PP from Guang-dong Canrd New Energy Technology Co., Ltd (Dongguan, China). The galvanostatic charge/discharge cycling and rate capability were carried out by using a battery testing system (2001A, LAND, Wuhan, China) in the voltage range of 0.01 to 3.0 V (vs. Li/Li<sup>+</sup>). Cyclic voltammetry (CV) test was carried out by using an electrochemical workstation (CS2350, Wuhan, China).

### 3. Results

A highly arrayed SnO<sub>2</sub> nanopillar architecture has been designed to overcome large volumetric change of SnO<sub>2</sub> (~300%) during the charge/discharge process. As schematically illustrated in Figure 1a, the fabrication process of SnO<sub>2</sub> array includes three steps: (1) AAO template transfer, (2) SnO<sub>2</sub> deposition, and (3) removal of AAO template. First, the AAO template is carefully transferred on Cu foil before SnO<sub>2</sub> deposition and then, the SnO<sub>2</sub> array is deposited on Cu foil by PLD using the AAO template. Finally, an array of highly ordered SnO<sub>2</sub> nanopillar is left on the Cu substrate after the removal of AAO template. The utilization of SnO<sub>2</sub> nanoarray as an anode material in LIBs is schematically presented in Figure 1b, where the Li-ion half-cell consists of lithium metal, the separator, and SnO<sub>2</sub> nanoarray. One should note that the highly arrayed SnO<sub>2</sub> nanopillar can provide enough room for volumetric change, abundant active sites for Li storage, and ordered electron transmission channels. Furthermore, the architecture of SnO<sub>2</sub> array is confirmed by scanning electronic microscopy (SEM), as shown in Figure 1c,d. The top-view SEM image in Figure 1c clearly demonstrates the morphology of AAO template before and after SnO<sub>2</sub> deposition, revealing the well-maintained AAO template structure during PLD. Moreover, the SEM image in Figure 1d confirms the array architecture of the SnO<sub>2</sub> nanopillar, wherein the diameter of SnO<sub>2</sub> nanopillar and the gap between neighboring SnO<sub>2</sub> nanopillar can be estimated as ~300 nm and ~130 nm, respectively, which are consistent with the structure of AAO template. Note that SnO<sub>2</sub> nanopillar with different diameter and gap were employed before we use the optimized diameter and gap as ~300 nm and ~130 nm, because we found that too small an array gap and the large nanopillar were unable to achieve long term charge/discharge cycling, which may cause by they unable to provide enough space to overcome the large volumetric change during the charge/discharge process.

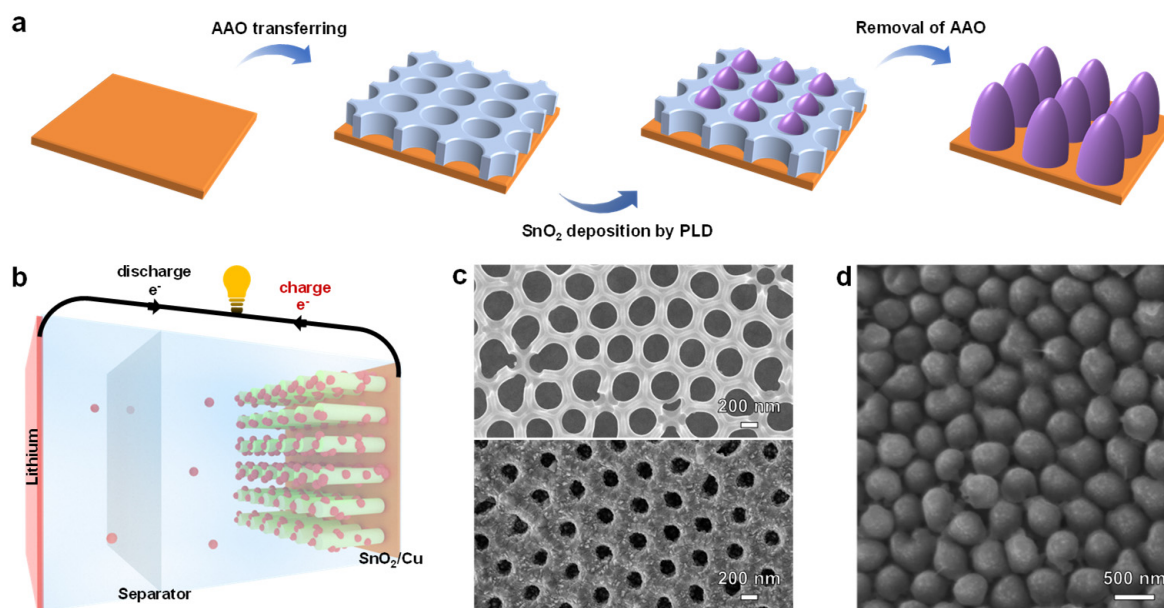


**Figure 1.** SnO<sub>2</sub> array deposition. (a) Fabrication of SnO<sub>2</sub> nanopillar array by PLD using AAO template on a Cu foil substrate; (b) Schematic diagram of a half-cell Li-ion battery, where SnO<sub>2</sub> nanoarray is used as an anode and Li-foil is used as a cathode and counter electrode; (c) SEM images of bare AAO template (upper panel) and AAO template after SnO<sub>2</sub> deposition (lower panel); and (d) a top-view SEM image of the SnO<sub>2</sub> nanopillar array after the removal of AAO template.

The X-ray diffraction (XRD) patterns of bare Cu foil and SnO<sub>2</sub>-coated Cu foil are presented in Figure 2a. The diffraction peaks can be well-indexed to tetragonal rutile-like SnO<sub>2</sub> structure without any impurities [25]. The chemical composition of SnO<sub>2</sub> nanoarray is further studied by X-ray photoelectron spectroscopy (XPS). The wide-range XPS spectrum is presented in Figure 2b, showing the presence of Sn, O and Cu elements. Note that the

silver (Ag) peak appeared due to the residual silver paste, which was used during XPS sample preparation. Moreover, the high-resolution XPS spectrum of Sn 3d is plotted in Figure 2c, wherein two peaks at around 495.3 eV and 486.4 eV correspond to Sn 3d<sub>3/2</sub> and Sn 3d<sub>5/2</sub> [26,27], respectively, confirming the +4 valence state of Sn and formation of pure SnO<sub>2</sub> phase [23]. The XPS data were further verified by energy dispersive spectroscopy (EDS). The elemental distribution of Sn, O and Cu is shown in Figure 2d-f. It can be readily observed that the Sn and O signals are prominent in the regions of nanopillar, whereas the Cu signal is relatively weaker. Overall, these results confirm the formation of a phase pure SnO<sub>2</sub> nanoarray architecture.

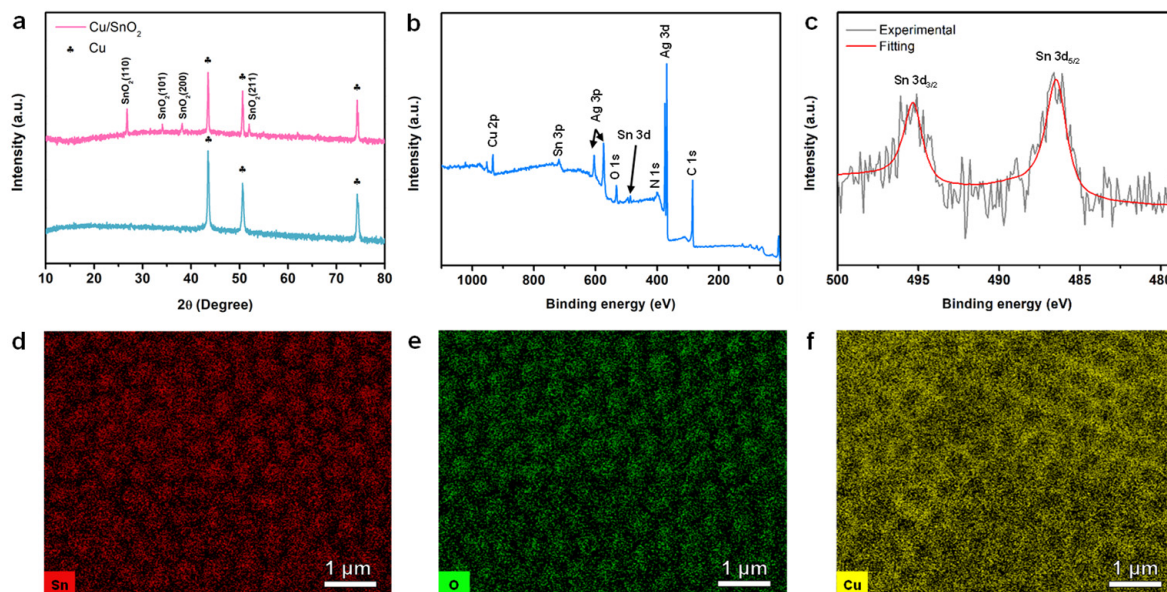
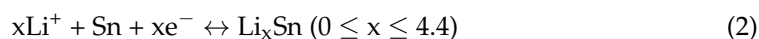
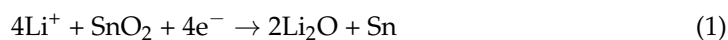


**Figure 2.** (a) XRD patterns of bare and SnO<sub>2</sub>-coated Cu foils; (b) wide-range XPS spectrum of SnO<sub>2</sub> nanoarray; (c) high-resolution Sn 3d XPS spectrum; and elemental maps of (d) Sn, (e) O and (f) Cu from SnO<sub>2</sub> nanoarray.

After structural and microstructural characterization, the cyclic voltammetry (CV) and galvanostatic charge/discharge testing were carried out to evaluate the electrochemical performance of SnO<sub>2</sub> nanoarray anode in LIBs. Also, the electrochemical performance of SnO<sub>2</sub> thin film is studied to demonstrate the positive influence of SnO<sub>2</sub> nanoarray architecture. The first three CV curves were recorded at the scan rate of 0.2 mV s<sup>-1</sup> in the voltage range of 0.01–3.0 V (vs. Li/Li<sup>+</sup>) to investigate the redox process in SnO<sub>2</sub> nanoarray architecture. During the first cathodic scan, as shown in Figure 3a, two reduction peaks located at ~1.27 and 0.87 V (vs. Li/Li<sup>+</sup>) correspond to the conversion reaction of SnO<sub>2</sub> to Sn (Equation (1)) and formation of solid electrolyte interphase (SEI), respectively [28,29]. Moreover, the peak at 0.18 V (vs. Li/Li<sup>+</sup>) is attributed to the alloying process of Sn with Li to form Li<sub>x</sub>Sn (Equation (2)) [30].



During the first anodic process, three oxidation peaks can be observed in Figure 3a, wherein the peak at ~0.51 V (vs. Li/Li<sup>+</sup>) indicates the dealloying reaction of Li<sub>x</sub>Sn (0 ≤ x ≤ 4.4) (Equation (2)) [31], the peak at ~1.25 V (vs. Li/Li<sup>+</sup>) represents the decomposition of Li<sub>x</sub>O, and the peak at ~1.91 V (vs. Li/Li<sup>+</sup>) corresponds to the reoxidation of Sn [32]. The redox peaks in Figure 3a confirm the cathodic and anodic processes of the SnO<sub>2</sub> nanoarray, which are consistent with previously reported SnO<sub>2</sub>-based anodes [20,25]. Moreover, the CV curves of SnO<sub>2</sub> thin film in Figure S1 (Supporting Information) show similar cathodic and anodic peaks, confirming the successful synthesis of phase pure

SnO<sub>2</sub> nanoarray. As shown in Figure 3a, the overlapping CV curves after the first cycle suggest the excellent reversibility of redox reactions during the charge/discharge process [11].

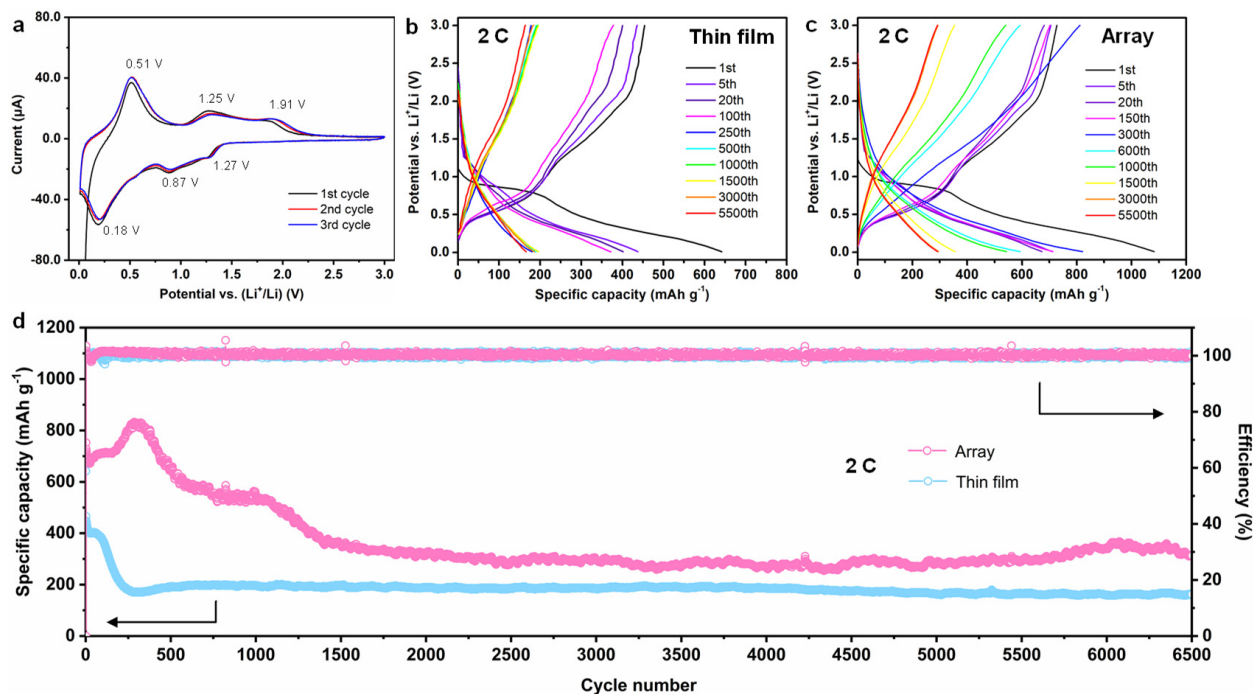


**Figure 3.** Electrochemical performance of SnO<sub>2</sub> electrodes. (a) CV curves of SnO<sub>2</sub> nanoarray at the scan rate of 0.2 mV s<sup>-1</sup>; charge/discharge profiles of (b) PLD-fabricated SnO<sub>2</sub> thin film and (c) SnO<sub>2</sub> nanoarray anodes at the current density of 2 C; and (d) cyclic performance of PLD-fabricated SnO<sub>2</sub> thin film and SnO<sub>2</sub> nanoarray at the current density of 2 C.

Furthermore, the discharge/charge voltage profiles of SnO<sub>2</sub> thin film and SnO<sub>2</sub> nanoarray anode are plotted in Figure 3b,c, respectively. During the first discharge process, an apparent characteristic plateau at ~1.0 V (vs. Li/Li<sup>+</sup>) is found (Figure 3b), which can be attributed to the irreversible occurrence of Equation (1) [25]. Moreover, a long slope due to the formation of Li<sub>x</sub>Sn (Equation (2)) appeared with the further discharge process. The initial specific capacity of SnO<sub>2</sub> thin film anode reached ~642 mAh g<sup>-1</sup>, which decreased to ~400 mAh g<sup>-1</sup> and ~200 mAh g<sup>-1</sup> after 100 and 250 cycles, respectively. The SnO<sub>2</sub> thin film anode rendered a stable specific capacity of ~200 mAh g<sup>-1</sup> from 250 to 6500 charge/discharge cycles. These results suggest that the utilization of SnO<sub>2</sub> thin film as an anode in LIBs leads to excellent cyclic performance with a moderate specific capacity, which lays a solid foundation for the outstanding performance of SnO<sub>2</sub> nanoarray anode. Indeed, as shown in Figure 3c, the discharge/charge plateaus of SnO<sub>2</sub> nanoarray anode during the first cycle are located at the same positions as SnO<sub>2</sub> thin film. Moreover, the initial discharge capacity of SnO<sub>2</sub> nanoarray reached 1082 mAh g<sup>-1</sup> and maintained at 700 mAh g<sup>-1</sup>, 600 mAh g<sup>-1</sup> and 300 mAh g<sup>-1</sup> after 300, 600, and 1500 charge/discharge cycles, respectively, suggesting a remarkable improvement in electrochemical performance and cyclic stability of SnO<sub>2</sub> nanoarray. As presented in Figure S2, the superior electrochemical performance can be attributed to the unique architecture of SnO<sub>2</sub>, where highly ordered SnO<sub>2</sub> nanopillar array provided adequate room for volumetric expansion and ensured structural integrity during the lithiation/delithiation process.

The excellent cyclic stability is further verified by carrying out charge/discharge cycling at the current density of 2 C (Figure 3d). In the case of SnO<sub>2</sub> thin film, the reversible specific capacity was first dropped from 642 mAh g<sup>-1</sup> to 402 mAh g<sup>-1</sup> after 20 discharge/charge cycles and then, the specific capacity was further dropped to about 180 mAh g<sup>-1</sup> during 100–250 discharge/charge cycles, which remained stable until the

6500th charge/discharge cycle. These results suggest that the SnO<sub>2</sub> thin film can be used as an anode, which renders a stable but moderate specific capacity. Furthermore, the highly arrayed SnO<sub>2</sub> nanopillar delivered long cycling performance and improved reversible specific capacity. As shown in Figure 3d, under the same current density of 2 C, the initial specific capacity of SnO<sub>2</sub> nanoarray was found to be 1082 mAh g<sup>-1</sup>, which dropped to 752 mAh g<sup>-1</sup> during the 2nd charge/discharge cycle.

Interestingly, the specific capacity increased to 832 mAh g<sup>-1</sup> at the 300th discharge/charge cycle after a slow decay, which is even higher than the 2nd reversible capacity. A possible reason for such an anomaly is that the thick SEI layer was exfoliated due to the high surface stress during the reactivation process. Subsequently, a fresh and thin SEI layer is formed [33], which can be partly confirmed from the detailed discussion of electrochemical impedance spectroscopy (Figure S3). The newly formed thin SEI layer is more stable than the previous thick SEI layer, which can bear severe volumetric change and fracture, resulting in improved Li storage capacity and longer cycling life [34]. Note that the stable charge-transfer resistance (*R*<sub>ct</sub>) of SnO<sub>2</sub> in Figure S3 reveals the well-maintained interface between SnO<sub>2</sub> nanoarray and substrate. Indeed, as shown in Figure 3d, the specific capacity of SnO<sub>2</sub> nanoarray gradually decreased and became stable at 524 mAh g<sup>-1</sup> during the 300th to 1100th charge/discharge cycles. The attained specific capacity is two times higher than the SnO<sub>2</sub> thin film. With further cycling, the reversible specific capacity stabilized at ~313 mAh g<sup>-1</sup> from 2000th to 6500th cycles, demonstrating the long cycling life and high capacity of binder-free SnO<sub>2</sub> nanoarray anode.

A range of current densities, i.e., 0.5 C to 16 C, was selected to investigate the cyclability of SnO<sub>2</sub> nanoarray and SnO<sub>2</sub> thin film anodes. Overall, the SnO<sub>2</sub> thin film delivered a lower discharge capacity than SnO<sub>2</sub> nanoarray, as shown in Figure 4a. In the case of SnO<sub>2</sub> thin film, the discharge specific capacity decreased with increasing current density from 440 mAh g<sup>-1</sup> at 0.5 C to 314 mAh g<sup>-1</sup> at 16 C. The SnO<sub>2</sub> thin film could not recover the initial capacity when the current density was reduced after high-rate cycling, which can be ascribed to structural failure of SnO<sub>2</sub> thin film. On the other side, the SnO<sub>2</sub> nanoarray anode rendered a high discharge capacity of 536 mAh g<sup>-1</sup> at 0.5 C and 414 mAh g<sup>-1</sup> at 16 C. More importantly, the SnO<sub>2</sub> nanoarray maintained a reversible capacity of 520 mAh g<sup>-1</sup> and 517 mAh g<sup>-1</sup>, under 1 C, after 100th and 160th cycles after high rate cycling at 16 C, indicating the excellent rate capability of nanoarray architecture. The difference in rate performance of the SnO<sub>2</sub> thin film and SnO<sub>2</sub> nanoarray can be attributed to the architectural differences, where the highly arrayed SnO<sub>2</sub> nanopillar enjoy enough space to alleviate volumetric expansion and ensure structural stability during the charge/discharge process.

Furthermore, we studied the rate capability of SnO<sub>2</sub> nanoarray at extremely high current densities, ranging from 2 C to 64 C. As shown in Figure 4b, the SnO<sub>2</sub> nanoarray delivered a specific capacity of 530, 471, 442, 398, and 354 mAh g<sup>-1</sup> at the current density of 2 C, 4 C, 8 C, 16 C, and 32 C during the 1st to 50th cycle, as well as a reversible specific capacity of 556, 498, 448, 404 and 354 mAh g<sup>-1</sup> at 2 C, 4 C, 8 C, 16 C and 32 C during 50th and 100th cycle, suggesting the high-rate capability of SnO<sub>2</sub> nanoarray. Moreover, at an ultrahigh current density of 64 C, the SnO<sub>2</sub> nanoarray delivered a specific capacity of ~278 mAh g<sup>-1</sup> during the 140th and 150th cycle (Figure 4b) and then, recovered a high specific capacity of 670 mAh g<sup>-1</sup> at the current density of 2 C (200th cycle). These results confirm that the SnO<sub>2</sub> nanoarray anode can work under ultrahigh current densities and possess remarkable rate capability. Lastly, the electrochemical performance of binder-free SnO<sub>2</sub> anode is compared with previously reported SnO<sub>2</sub>-based anodes [14,24,31,35–37], as shown in Figure 4c, demonstrating the superior Li storage capacity and high-rate capability of the as-fabricated SnO<sub>2</sub> nanoarray. The superior electrochemical performance of SnO<sub>2</sub> nanoarray can be attributed to the unique architecture of SnO<sub>2</sub>, where highly ordered SnO<sub>2</sub> nanopillar array provided adequate room for volumetric expansion and ensured structural integrity during the lithiation/delithiation process. It also should note that the other two points may also play important role for our SnO<sub>2</sub> nanoarray to resist the 300% volumetric change during charge/discharge process. First, we fabricate SnO<sub>2</sub> nanopillar based on

PLD can ensure excellent contact between SnO<sub>2</sub> and Cu, but it will also bring a strong substrate constraint from the Cu substrate to SnO<sub>2</sub>, which will greatly clamp the volume expansion of SnO<sub>2</sub> along lateral direction, making the volumetric change less than 300%. Moreover, the obtained SnO<sub>2</sub> nanopillars usually are not in uniform cylindrical shape when we use AAO-assisted PLD, as we schematic shown in Figure 1a, the top parts (away from interface of SnO<sub>2</sub> and Cu) of SnO<sub>2</sub> nanopillars usually prefer to appear in pyramid shape, such unique architecture provide more room and multiple routes for the expansion of SnO<sub>2</sub> nanopillars.

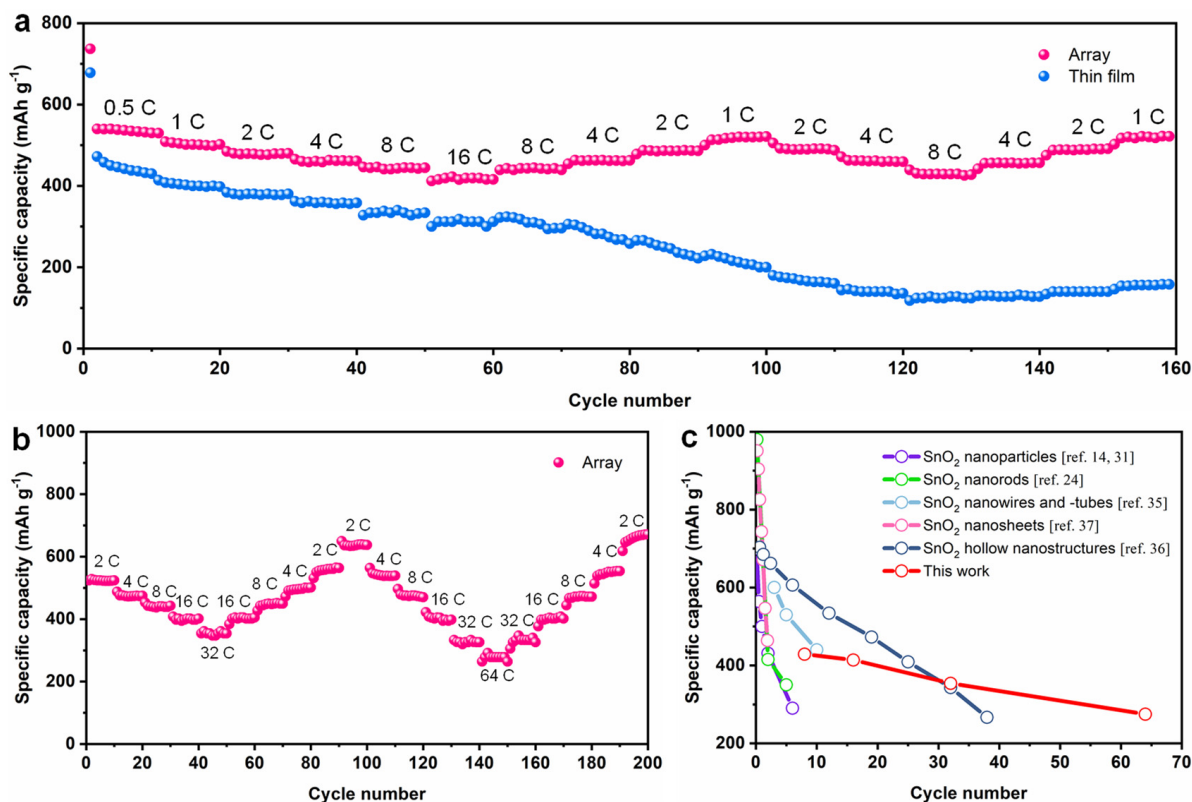


**Figure 4.** Rate performance of SnO<sub>2</sub> nanoarray and SnO<sub>2</sub> thin films. (a) The rate capability of SnO<sub>2</sub> nanoarray and PLD-fabricated SnO<sub>2</sub> thin film at different current densities, ranging from 0.5 C to 16 C; (b) rate capability of SnO<sub>2</sub> nanoarray at different current densities, ranging from 2 C to 64 C; and (c) comparison of the electrochemical performance for SnO<sub>2</sub>-based anodes.

#### 4. Conclusions

In summary, we have fabricated a well-oriented and binder-free SnO<sub>2</sub> nanopillar array as an anode electrode for LIBs. The as-synthesized SnO<sub>2</sub> nanoarray anode rendered superior Li storage capacity of 1082 mAh g<sup>-1</sup> and excellent cyclic stability (~313 mAh g<sup>-1</sup> after 6500 charge/discharge cycles). Moreover, the SnO<sub>2</sub> nanoarray demonstrated ultrahigh rate capability, i.e., the capacity of ~278 mAh g<sup>-1</sup> at the current density of 64 C, outperforming the previously reported binder-free SnO<sub>2</sub>-based anodes. The superior electrochemical performance of SnO<sub>2</sub> nanoarray can be attributed to the unique architecture of SnO<sub>2</sub>, where the highly arrayed SnO<sub>2</sub> nanopillar provided adequate room for volumetric expansion and ensured structural integrity during the lithiation/delithiation process. The fabrication of SnO<sub>2</sub> nanoarray presents an effective approach to enhance the energy density and rapid charge/discharge capability of LIBs.

**Supplementary Materials:** The following are available online at <https://www.mdpi.com/article/10.3390/nano11051307/s1>, Figure S1: Cyclic voltammetry curves of SnO<sub>2</sub> thin films at scan rate 0.2 mV s<sup>-1</sup>, Figure S2: Top-view SEM images. (a,b) the top-view SEM images of as-deposited (a)

SnO<sub>2</sub> thin film and (b) after 5 discharge/charge cycles; (c,d) the top-view SEM images of as-deposited (c) SnO<sub>2</sub> nanopillar array and (d) after 5 discharge/charge cycles, Figure S3: (a,b) the nyquist plots of SnO<sub>2</sub> nanoarray (a) and thin film (b) at 20th, 50th, 400th cycles.

**Author Contributions:** L.D.: Methodology, Investigation, Resources, Data analysis, Writing-original draft, Writing-review & editing. X.Z.: Investigation, Supervision. J.Z.: Data analysis, Investigation. B.F.: Data analysis, Investigation. Y.S.: Data analysis, Investigation. C.R.: Data analysis, Investigation. J.W.: Investigation, Supervision. G.Z.: Conceptualization, Funding acquisition, Project administration, Supervision, Writing-original draft, Writing-review & editing. All authors have read and agreed to the published version of the manuscript.

**Funding:** This work was supported by the National Natural Science Foundation of China (No. 51902337, No. 92066102, No. 11875229), Shenzhen Science and Technology Innovation Committee (Nos. KQTD20170810160424889, Nos. RCYX20200714114733204), Shenzhen Institute of Advanced Technology, Chinese Academy of Sciences (No. Y9G050).

**Data Availability Statement:** The data presented in this study are available on request from the corresponding author.

**Conflicts of Interest:** The authors declare that they have no known competing financial interests or personal relationships that could have appeared to influence the work reported in this paper.

## References

1. Zhang, D.; Xu, X.; Qin, Y.; Ji, S.; Huo, Y.; Wang, Z.; Shen, J.; Liu, J. Recent progress in organic-inorganic composite solid electrolytes for all-solid-state lithium batteries. *Chem. Eur. J.* **2020**, *26*, 1720–1736. [[CrossRef](#)] [[PubMed](#)]
2. Tarascon, J.-M.; Reham, N.; Armand, M.; Chotard, J.-N.; Barpanda, P.; Walker, W.; Dupont, L. Hunting for Better Li-Based Electrode Materials via Low Temperature Inorganic Synthesis. *Chem. Mater.* **2010**, *22*, 724–739. [[CrossRef](#)]
3. Sui, Y.; Liu, C.; Masse, R.C.; Neale, Z.G.; Atif, M.; AlSalhi, M.; Cao, G. Dual-ion batteries: The emerging alternative rechargeable batteries. *Energy Storage Mater.* **2020**, *25*, 1–32. [[CrossRef](#)]
4. Huang, X.; Yu, H.; Chen, J.; Lu, Z.; Yazami, R.; Hng, H.H. Ultrahigh Rate Capabilities of Lithium-Ion Batteries from 3D Ordered Hierarchically Porous Electrodes with Entrapped Active Nanoparticles Configuration. *Adv. Mater.* **2014**, *26*, 1296–1303. [[CrossRef](#)]
5. Jiang, Y.; Hu, M.; Zhang, D.; Yuan, T.; Sun, W.; Xu, B.; Yan, M. Transition metal oxides for high performance sodium ion battery anodes. *Nano Energy* **2014**, *5*, 60–66. [[CrossRef](#)]
6. Zheng, M.; Tang, H.; Li, L.; Hu, Q.; Zhang, L.; Xue, H.; Pang, H. Hierarchically Nanostructured Transition Metal Oxides for Lithium-Ion Batteries. *Adv. Sci.* **2018**, *5*, 1700592. [[CrossRef](#)]
7. Zhong, G.; Qu, K.; Ren, C.; Su, Y.; Fu, B.; Zi, M.; Dai, L.; Xiao, Q.; Xu, J.; Zhong, X.; et al. Epitaxial array of Fe<sub>3</sub>O<sub>4</sub> nanodots for high rate high capacity conversion type lithium ion batteries electrode with long cycling life. *Nano Energy* **2020**, *74*, 104876. [[CrossRef](#)]
8. Wu, Z.S.; Ren, W.; Wen, L.; Gao, L.; Zhao, J.; Chen, Z.; Zhou, G.; Li, F.; Cheng, H.M. Graphene anchored with Co<sub>3</sub>O<sub>4</sub> nanoparticles as anode of lithium ion batteries with enhanced reversible capacity and cyclic performance. *ACS Nano* **2010**, *4*, 3187–3194. [[CrossRef](#)]
9. Hu, R.; Ouyang, Y.; Liang, T.; Wang, H.; Liu, J.; Chen, J.; Zhu, M. Stabilizing the nanostructure of SnO<sub>2</sub> anodes by transition metals: A route to achieve high initial coulombic efficiency and stable capacities for lithium storage. *Adv. Mater.* **2017**, *29*, 1605006. [[CrossRef](#)]
10. Courtney, I.A.; Dahn, J.R. Electrochemical and in situ X-ray diffraction studies of the reaction of lithium with tin oxide composites. *J. Electrochem. Soc.* **1997**, *144*, 2045–2052. [[CrossRef](#)]
11. Zhou, X.; Wan, L.-J.; Guo, Y.-G. Binding SnO<sub>2</sub> Nanocrystals in Nitrogen-Doped Graphene Sheets as Anode Materials for Lithium-Ion Batteries. *Adv. Mater.* **2013**, *25*, 2152–2157. [[CrossRef](#)] [[PubMed](#)]
12. Idota, Y.; Kubota, T.; Matsufuji, A.; Maekawa, Y.; Miyasaka, T. Tin-Based Amorphous Oxide: A High-Capacity Lithium-Ion-Storage Material. *Science* **1997**, *276*, 1395–1397. [[CrossRef](#)]
13. Ng, S.; dos Santos, D.; Chew, S.; Wexler, D.; Wang, J.; Dou, S.; Liu, H. Polyol-mediated synthesis of ultrafine tin oxide nanoparticles for reversible Li-ion storage. *Electrochem. Commun.* **2007**, *9*, 915–919. [[CrossRef](#)]
14. Etacheri, V.; Seisenbaeva, G.A.; Caruthers, J.; Daniel, G.; Nedelec, J.-M.; Kessler, V.G.; Pol, V.G. Ordered Network of Interconnected SnO<sub>2</sub> Nanoparticles for Excellent Lithium-Ion Storage. *Adv. Energy Mater.* **2015**, *5*, 1401289. [[CrossRef](#)]
15. Wang, H.-G.; Wu, Q.; Wang, Y.; Wang, X.; Wu, L.; Song, S.; Zhang, H. Molecular Engineering of Monodisperse SnO<sub>2</sub> Nanocrystals Anchored on Doped Graphene with High-Performance Lithium/Sodium-Storage Properties in Half/Full Cells. *Adv. Energy Mater.* **2019**, *9*, 1802993. [[CrossRef](#)]
16. Zhong, G.; Bitla, Y.; Wang, J.; Zhong, X.; An, F.; Chin, Y.-Y.; Zhang, Y.; Gao, W.; Zhang, Y.; Eshghinejad, A.; et al. Tuning Fe concentration in epitaxial gallium ferrite thin films for room temperature multiferroic properties. *Acta Mater.* **2018**, *145*, 488–495. [[CrossRef](#)]
17. Li, Z.; Wang, Y.; Tian, G.; Li, P.; Zhao, L.; Zhang, F.; Yao, J.; Fan, H.; Song, X.; Chen, D.; et al. High-density array of ferroelectric nanodots with robust and reversibly switchable topological domain states. *Sci. Adv.* **2017**, *3*, e1700919. [[CrossRef](#)]

18. Zhong, G.; An, F.; Bitla, Y.; Wang, J.; Zhong, X.; Ye, M.; Zhang, Y.; Gao, W.; Pan, X.; Xie, S.; et al. Self-assembling epitaxial growth of a single crystalline  $\text{CoFe}_2\text{O}_4$  nanopillar array via dual-target pulsed laser deposition. *J. Mater. Chem. C* **2018**, *6*, 4854–4860. [[CrossRef](#)]
19. Chen, S.; Wang, M.; Ye, J.; Cai, J.; Ma, Y.; Zhou, H.; Qi, L. Kinetics-controlled growth of aligned mesocrystalline  $\text{SnO}_2$  nanorod arrays for lithium-ion batteries with superior rate performance. *Nano Res.* **2013**, *6*, 243–252. [[CrossRef](#)]
20. Park, M.-S.; Wang, G.-X.; Kang, Y.-M.; Wexler, D.; Dou, S.-X.; Liu, H.-K. Preparation and Electrochemical Properties of  $\text{SnO}_2$  Nanowires for Application in Lithium-Ion Batteries. *Angew. Chem. Int. Ed.* **2007**, *46*, 750–753. [[CrossRef](#)]
21. Ying, Z.; Wan, Q.; Cao, H.; Song, Z.T.; Feng, S.L. Characterization of  $\text{SnO}_2$  nanowires as an anode material for Li-ion batteries. *Appl. Phys. Lett.* **2005**, *87*, 113108. [[CrossRef](#)]
22. Wang, Y.; Lee, J.Y.; Zeng, H.C. Polycrystalline  $\text{SnO}_2$  Nanotubes Prepared via Infiltration Casting of Nanocrystallites and Their Electrochemical Application. *Chem. Mater.* **2005**, *17*, 3899–3903. [[CrossRef](#)]
23. Hwang, S.M.; Lim, Y.-G.; Kim, J.-G.; Heo, Y.-U.; Lim, J.H.; Yamauchi, Y.; Park, M.-S.; Kim, Y.-J.; Dou, S.X.; Kim, J.H. A case study on fibrous porous  $\text{SnO}_2$  anode for robust, high-capacity lithium-ion batteries. *Nano Energy* **2014**, *10*, 53–62. [[CrossRef](#)]
24. Liu, J.; Li, Y.; Huang, X.; Ding, R.; Hu, Y.; Jiang, J.; Liao, L. Direct growth of  $\text{SnO}_2$  nanorod array electrodes for lithium-ion batteries. *J. Mater. Chem.* **2009**, *19*, 1859–1864. [[CrossRef](#)]
25. Park, M.-S.; Kang, Y.-M.; Wang, G.-X.; Dou, S.-X.; Liu, H.-K. The Effect of Morphological Modification on the Electrochemical Properties of  $\text{SnO}_2$  Nanomaterials. *Adv. Funct. Mater.* **2008**, *18*, 455–461. [[CrossRef](#)]
26. Liu, X.; Jiang, Y.; Li, K.; Xu, F.; Zhang, P.; Ding, Y. Electrospun free-standing N-doped  $\text{C@SnO}_2$  anode paper for flexible Li-ion batteries. *Mater. Res. Bull.* **2019**, *109*, 41–48. [[CrossRef](#)]
27. Aravindan, V.; Jinesh, K.; Prabhakar, R.R.; Kale, V.S.; Madhavi, S. Atomic layer deposited (ALD)  $\text{SnO}_2$  anodes with exceptional cycleability for Li-ion batteries. *Nano Energy* **2013**, *2*, 720–725. [[CrossRef](#)]
28. Li, N.; Martin, C.R. A High-Rate, High-Capacity, Nanostructured Sn-Based Anode Prepared Using Sol-Gel Template Synthesis. *J. Electrochem. Soc.* **2001**, *148*, A164–A170. [[CrossRef](#)]
29. Shi, W.; Lu, B. Nanoscale Kirkendall effect synthesis of echinus-like  $\text{SnO}_2@\text{SnS}_2$  nanospheres as high-performance anode material for lithium ion batteries. *Electrochim. Acta* **2014**, *133*, 247–253. [[CrossRef](#)]
30. Lin, J.; Peng, Z.; Xiang, C.; Ruan, G.; Yan, Z.; Natelson, D.; Tour, J.M. Graphene Nanoribbon and Nanostructured  $\text{SnO}_2$  Composite Anodes for Lithium Ion Batteries. *ACS Nano* **2013**, *7*, 6001–6006. [[CrossRef](#)]
31. Yin, L.; Chai, S.; Wang, F.; Huang, J.; Li, J.; Liu, C.; Kong, X. Ultrafine  $\text{SnO}_2$  nanoparticles as a high performance anode material for lithium ion battery. *Ceram. Int.* **2016**, *42*, 9433–9437. [[CrossRef](#)]
32. Ferraresi, G.; Villeveille, C.; Czekaj, I.; Horisberger, M.; Novák, P.; El Kazzi, M.  $\text{SnO}_2$  Model Electrode Cycled in Li-Ion Battery Reveals the Formation of  $\text{Li}_2\text{SnO}_3$  and  $\text{Li}_8\text{SnO}_6$  Phases through Conversion Reactions. *ACS Appl. Mater. Interfaces* **2018**, *10*, 8712–8720. [[CrossRef](#)]
33. Nadimpalli, S.P.V.; Sethuraman, V.A.; Bucci, G.; Srinivasan, V.; Bower, A.F.; Guduru, P.R. On Plastic Deformation and Fracture in Si Films during Electrochemical Lithiation/Delithiation Cycling. *J. Electrochem. Soc.* **2013**, *160*, A1885–A1893. [[CrossRef](#)]
34. Sun, H.; Xin, G.; Hu, T.; Yu, M.; Shao, D.; Sun, X.; Lian, J. High-rate lithiation-induced reactivation of mesoporous hollow spheres for long-lived lithium-ion batteries. *Nat. Commun.* **2014**, *5*, 4526. [[CrossRef](#)]
35. Ko, Y.-D.; Kang, J.-G.; Park, J.-G.; Lee, S.; Kim, D.-W. Self-supported  $\text{SnO}_2$  nanowire electrodes for high-power lithium-ion batteries. *Nanotechnology* **2009**, *20*, 455701. [[CrossRef](#)] [[PubMed](#)]
36. Park, G.D.; Lee, J.-K.; Kang, Y.C. Synthesis of Uniquely Structured  $\text{SnO}_2$  Hollow Nanoplates and Their Electrochemical Properties for Li-Ion Storage. *Adv. Funct. Mater.* **2016**, *27*, 1603399. [[CrossRef](#)]
37. Zhu, Y.; Guo, H.; Zhai, H.; Cao, C. Microwave-Assisted and Gram-Scale Synthesis of Ultrathin  $\text{SnO}_2$  Nanosheets with Enhanced Lithium Storage Properties. *ACS Appl. Mater. Interfaces* **2015**, *7*, 2745–2753. [[CrossRef](#)] [[PubMed](#)]